Lawrence Berkeley National Laboratory

LBL Publications

Title

Hierarchical median narrow band for level set segmentation of cervical cell nuclei

Permalink

https://escholarship.org/uc/item/0wr4p6zq

Authors

Braga, Alan M

Marques, Regis CP

Medeiros, Fátima NS

et al.

Publication Date

2021-05-01

DOI

10.1016/j.measurement.2021.109232

Peer reviewed

eScholarship.org Powered by the California Digital Library
University of California

Hierarchical Median Narrow Band for Level Set Segmentation of Cervical Cell Nuclei

Alan M. Braga[a,b,*], Regis C. P. Marques[a], Fátima N. S. Medeiros[b], Jeová F. S. Rocha Neto[c], Andrea G. C. Bianchi[d], Claudia M. Carneiro[d], Daniela M. Ushizima[e,f]

[a]*Federal Institute of Ceará, Fortaleza, Ceará, Brazil*
[b]*Federal University of Ceará, Fortaleza, Ceará, Brazil*
[c]*Brown University, Providence, RI, USA*
[d]*Federal University of Ouro Preto, Ouro Preto, Minas Gerais, Brazil*
[e]*Berkeley Institute for Data Science, University of California, Berkeley, CA, USA*
[f]*Lawrence Berkeley National Laboratory, Berkeley, CA, USA*

Abstract

This paper presents a novel hierarchical nuclei segmentation algorithm for isolated and overlapping cervical cells based on a narrow band level set implementation. Our method applies a new multiscale analysis algorithm to estimate the number of clusters in each image region containing cells, which turns into the input to a narrow band level set algorithm. We assess the nuclei segmentation results on three public cervical cell image databases. Overall, our segmentation method outperformed six state-of-the-art methods concerning the number of correctly segmented nuclei and the Dice coefficient reached values equal to or higher than 0.90. We also carried out classification experiments using features extracted from our segmentation results and the proposed pipeline achieved the highest average accuracy values equal to 0.89 and 0.77 for two-class and three-class problems, respectively. These results demonstrated the suitability of the proposed segmentation algorithm to integrate decision support systems for cervical cell screening.

Keywords: cervical cell, cluster estimation, hierarchical algorithm, narrow band level set, nuclei segmentation.

1. Introduction

Cervical cancer no longer occupies a visible place on the list of diseases dreaded by Western women [1], however it is estimated that over a million women worldwide currently suffers from this disease [2]. Over the past three decades, cervical cancer rates have decreased in most developed countries, mainly due to

*Corresponding author
Email addresses: alanmbraga@gmail.com (Alan M. Braga), regismarques@ifce.edu.br (Regis C. P. Marques), fsombra@ufc.br (Fátima N. S. Medeiros), jeova_farias@brown.edu (Jeová F. S. Rocha Neto), andrea@iceb.ufop.br (Andrea G. C. Bianchi), carneirocm@gmail.com (Claudia M. Carneiro), dushizima@lbl.gov (Daniela M. Ushizima)

the effectiveness of the Papanicolaou screening test (Pap smear test) [2]. In this test, cytologists, using a microscope, search for very early changes in the uterine cervix cells (also called pre-cancer), before cancer develops [2, 3].

Recent works [4, 5, 6, 7, 8, 9] have focused on automatic cell analysis, including more accurate segmentation methods for microscopy images, since the visual interpretation is time-consuming and requires high-level experienced observers [10]. Furthermore, changes in the cell nucleus morphology, nuclear texture and hyperchromasia are highly informative to recognize abnormal cells [11, 12, 13]. In cell classification tasks, information about nucleus plays a key role because it may reveal significant changes in shape and chromatin distribution [14, 15, 16]. Thus, efficient and accurate methods for nuclei segmentation are decisive to design reliable computational tools for cervical cancer screening.

Although nucleus, cytoplasm and background are the three main regions in cervical cells, Pap test images may contain blood cells, inflammatory cells, cell fragments, debris, overlapping cells, etc. In addition, changes caused by Human Papilloma Virus (HPV) can generate dense cell clusters. This is a challenging scenario where multiregion segmentation is required and level set is an efficient approach to handle it. The original level set provides binary segmentation and it is a robust and accurate method for image segmentation [17] of a wide range of applications. For example, Rebouças *et al.* [18] introduced an algorithm for graphite nodule segmentation and Alarifi and Alwadain [19] proposed a level set algorithm to detect dental cancer. Wu and He [20] proposed a variational level set model and a pointwise convergent numerical scheme for the purpose of two-phase segmentation. Liu *et al.* [21] proposed a variational model in a binary level set framework for segmenting two-phase images with impulse noise. Nevertheless, the original level set formulation is computationally expensive and to overcome this drawback Ushizima *et al.* [22] used the fast marching method [17] for vessel segmentation. This method is faster and shares a common theory and numerical methodology with the level set method. However, the fast marching embodies a curve that advances only monotonically, i.e., forward or backward. Our proposed algorithm has the advantage of moving a curve in both directions to delimit a region of interest. Thus, we adopted a fast binary level set, introduced by Braga *et al.* [23], with a narrow band implementation [17]. The main reason for this new implementation is that it reduces the computational cost as it performs only in a narrow band of the propagation curve.

The generalization of the original level set to multiple regions usually comprises several level set functions. However, according to [24], the design of efficient propagation models for multi-region segmentation is a hard task when the number of regions is unknown. For instance, global level set approaches driven by subtle contrast differences between cytoplasm regions and nuclei tend to misclassify the nuclear regions. Undesirable

results may occur such as the intersection of regions or sets of regions which do not cover the image domain. Alternatively, hierarchical level set methods can perform multi-region segmentation [25, 26].

Inspired by [26], our hierarchical algorithm for nuclei segmentation recursively processes the whole image and outputs two new regions. The hierarchical segmentation criterion is based on a multiscale analysis over each region histogram to estimate the number of clusters for the next splitting step. Henceforth, the algorithm performs image segmentation if the current region comprises two or more clusters. Thus, at each step of the hierarchical process, it searches for cell nuclei based on six features of the segmented regions: size, mean gray level, difference between mean gray level and neighborhood gray level, circularity, minor and major axis ratio and area ratio between nucleus and cytoplasm. The main contributions of this work are as follows: (a) development of a novel hierarchical narrow band level set algorithm for cervical cell nuclei segmentation that does not rely on prior information about the number of image clusters; (b) implementation of the median filter regularized level set algorithm proposed in [23] in narrow band, here called median narrow band level set; (c) design of a new multiscale method for cluster estimation to support the hierarchical process and to initialize the median narrow band level set algorithm.

In this paper, we carried out experiments on images from three public cervical cell databases presented in [6] (Extended Depth of Field (EDF) images), [27] (ISBI 2014 challenge) and [28] (Herlev) and appraise the accuracy of six cervical cell segmentation methods. In addition, we assess the accuracy and impact of the segmentation results on classification tasks, that rely on feature extraction, using the Herlev data set that contains labelling information about the cell images. Hence, based on texture and shape features obtained from the nuclei segmentation results, we perform classification experiments into two classes (normal and abnormal) and three classes (normal, Low-grade Squamous Intraepithelial Lesion (LSIL) and High-grade Squamous Intraepithelial Lesion (HSIL)) in accordance with the Bethesda system which is used for diagnosis. Overall, our segmentation results promote a set of features extracted from cell nuclei quite similar to the ones extracted from the ground truth images, in cervical cell classification experiments. It means that accurate nuclei segmentation preserves and encompasses intrinsic shape and texture differences among cells. Furthermore, the proposed algorithm deals with three cell image databases that present remarkable differences concerning resolution, contrast, imaging source, images with single cells and clump of cells with different degrees of overlap real and synthetic images, to name a few.

The paper unfolds as follows: Section 2 presents the related works. Section 3 introduces the hierarchical narrow band level set algorithm for nuclei segmentation and the multiscale algorithm for cluster detection. In Section 4, we perform the comparative evaluation of the proposed approach with the methods introduced

by [6], [29], [30], [31], [3] and [32]. Section 5 presents the results, evaluates and discusses them. Finally, Section 6 draws conclusions and future developments.

2. Related Work

Efforts to apply multiple level set functions for cervical cell segmentation [6] enabled the analysis of nuclei and cytoplasm from both free-lying and overlapping cells. Lu *et al.* [6] obtained a super-pixel image using the quick shift algorithm. Then, it detected edges and builded a convex hull. In order to achieve the final regions of cell clumps, the algorithm performed an unsupervised binary classification. These cell clumps are used as inputs to the Maximally Stable Extremal Regions (MSER) algorithm to detect stable connected components that contain the nuclei. Finally, to obtain the individual cytoplasm regions, the detected nuclei are used to estimate the initial segmentation and the shape prior to the subsequent level set optimization. Here, we further refer to this cell segmentation method as MSERLS. Ushizima *et al.* [29] developed an algorithm for cell clump segmentation by merging regions based on pixel adjacency and intensity similarity using a graph-based algorithm, followed by a global search cutoff approach on the superpixel image. Here, we named this algorithm LTSN. It applies a local thresholding algorithm to segment nuclei inside cell clumps and, based on the identified nuclei, it divides the image into convex polygons through Voronoi diagrams to separate overlapping cytoplasm.

The Radiating Gradient Vector Flow snake (RGVF) [30] method achieved relevant results on images with single cervical cells. This method roughly divides an image into nucleus, cytoplasm and background regions by using a spatial K-means algorithm and the contours extracted from these initial results are the inputs for the RGVF snake [30]. Chankong *et al.* [31] introduced a cell segmentation method that combines the fuzzy C-means (FCM) clustering technique and a median filtering step, and hence we named it MFCM. FCM is responsible for dividing the filtered image into 7 clusters which are classified into three final clusters, i.e., nucleus, cytoplasm, and background.

More recent cervical cell nuclei segmentation algorithms based on deep learning [3, 33, 34, 35, 36] are available in literature. The main drawbacks of these algorithms are the reliance on a large number of images for training and the high computational cost. Tareef *et al.* [3] designed an automatic algorithm based on deep learning and dynamic shape model for individual nuclei and cytoplasm segmentation from Pap smear images. The simple linear iterative clustering technique (SLIC) [37] generates image patches or superpixels taking into account the intensity similarities and spatial proximity. Then, it classifies the image patches into three cellular components, i.e., nuclei, cytoplasmic mass, and background using a convolutional neural

network (CNN). The level set algorithm refines the contours of regions. It separates the individual cytoplasm, for each detected nucleus, inside each cellular mass in a variational segmentation framework with a learned shape that is iteratively updated. Here, we further refer to this cell segmentation method as DeepCNN1. Gautam *et al.* [32] proposed a new approach for nuclei segmentation based on selective pre-processing. This approach provides image patches to deep convolutional neural networks for pixel-wise 3 class labelling as nucleus, edge or background. This nuclei segmentation approach was named here DeepCNN2.

3. Proposed Hierarchical Algorithm for Nuclei Segmentation

The proposed nuclei segmentation algorithm, named hierarchical median narrow band level set algorithm (HMLS), follows the scheme displayed in Figure 1. It starts splitting the input image, i.e., a cervical cell image, into foreground (cellular mass) and background regions by using the binary median level set [23] with a narrow band implementation, called median narrow band level set, where the data are updated only within a narrow band around the curve, as Figure 2 shows. Then, each cellular mass segment is, recursively, partitioned into new ones which are inputs again for the median narrow band level set. Our hierarchical algorithm also provides a new multiscale cluster detection algorithm for the median narrow band level set initialization and to guide the hierarchical division process. Figure 3 exhibits the steps of the cluster detection algorithm.

The proposed hierarchical algorithm for nuclei segmentation uses the same binary median level set, but implemented in narrow band [17], of the hierarchical algorithm in [23], which was proposed for multi-region segmentation of synthetic aperture radar (SAR) images. In this algorithm, the stopping condition is based on the arithmetic–geometric distance and the propagation function is based on the G_I^0 distribution. Here, we use the information from the cluster detection algorithm in the stopping criterion and the front propagation of the narrow band level set evolves according to the likelihood function based on the Gaussian distribution.

Based on the nuclei segmentation results, we can compute shape and texture features for classification experiments in image databases that contain the true class labels for each sample image. Although the proposed method was developed for cervical cell nuclei segmentation, this classification stage can be used to assess the accuracy and impact of the segmentation results on cell image classification. In this paper, we classify the cervical cells into two and three classes, in accordance with the Bethesda system used for diagnosis. We calculated the average values of the classification measures, presented in Section 4.1, by carrying out 100 executions, where for each execution, we have divided, randomly, the data set into two independent subsets, i.e., the training set with 70% of data and the test set with 30% of data.

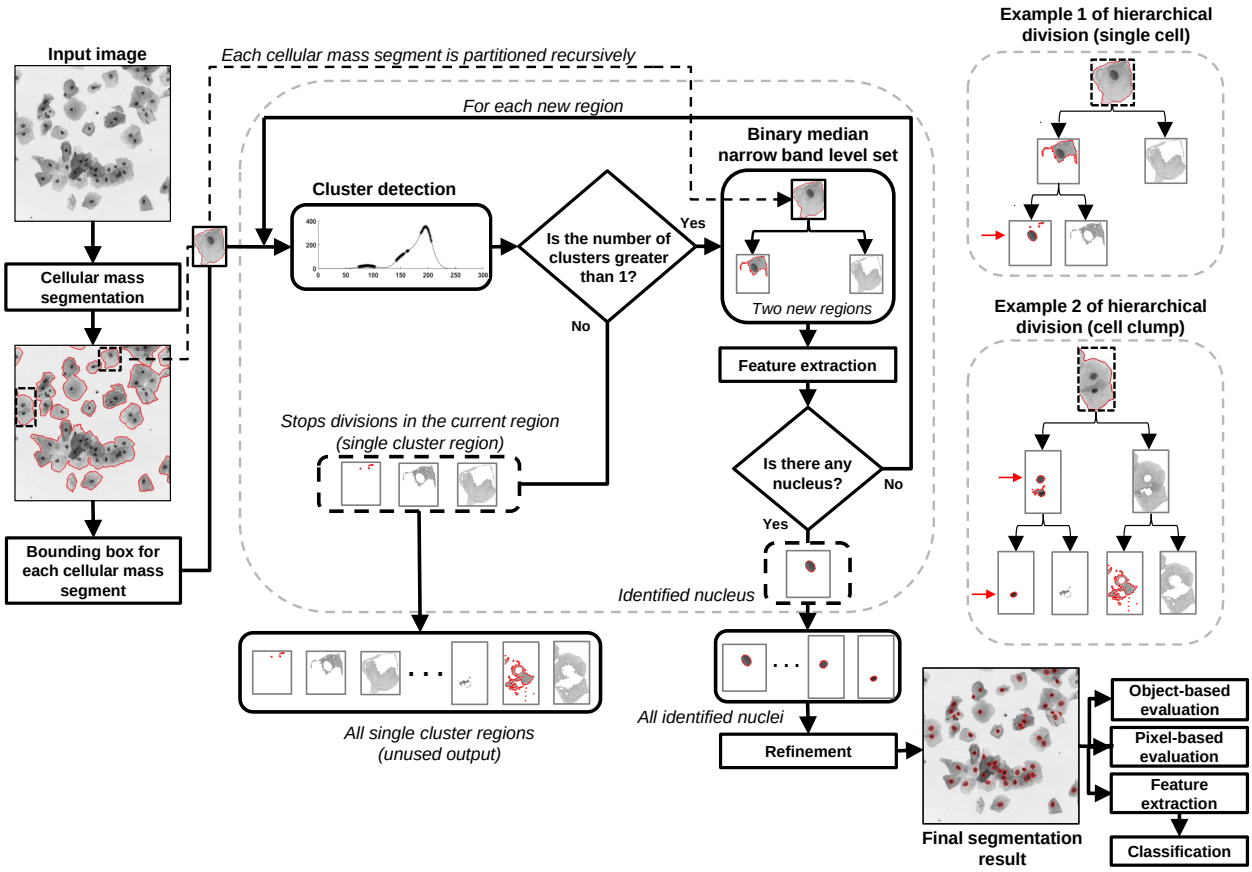

Figure 1: Flowchart of the proposed hierarchical median narrow band level set (HMLS). In the illustrations that contain single cell or clump of cells, the white regions are not considered in the current division and the arrows, in examples 1 and 2 of the hierarchical division, indicate that the segments are identified as nuclei.

3.1. Median Narrow Band Level Set

The level set theory in [17] states that a closed curve $\vec{\phi} : \mathbb{R}^2 \times \mathbb{R}^+ \rightarrow \mathbb{R}$ evolves with a velocity field $(\pm F\vec{\eta})$, where $(\pm\vec{\eta})$ is the unit vector that is perpendicular to $\vec{\phi}$. The movement of this curve is a consequence of the surface $\psi(\mathbf{x})$ motion, in which one is embedded in accordance with:

$$\vec{\phi}(s) = \{\mathbf{x} | \psi(\mathbf{x}) = 0\},\ \mathbf{x} \in \mathbb{R}^n, \tag{1}$$

where $s \in \mathbb{R}^2$ is the coordinate of the parametric curve $\vec{\phi}$. In the discrete domain, this process is expressed as

$$\psi^{k+1} = \psi^k + \triangle t \times (F + \varepsilon\mathcal{K}) \cdot |\nabla\psi^k|, \tag{2}$$

where ψ^k is the level set function, $\triangle t$ is the time step, and $|\nabla\psi^k|$ stands for the gradient magnitude. The two speed terms refer to the front regularization $\varepsilon\mathcal{K}$ and propagation $F = \frac{d\vec{\phi}}{dt}$, where F should minimize a cost function.

The numerical implementation of Eq. (2) is given by [17]

$$\psi^{k+1} = \psi^k - \Delta t \times \left(\max(F,0)\Delta^+ + \min(F,0)\Delta^- + \varepsilon\mathcal{K}\left|\nabla\psi^k\right|\right), \tag{3}$$

where Δ^+ and Δ^- are the forward and backward derivatives of ψ^k, respectively.

The implementation of the narrow band level set in [17] enables it to update data only in the neighborhood of the curve, which can greatly reduce the computational cost. Here, we use the fast binary level set algorithm proposed in [23] with the narrow band implementation introduced in [17]. This fast level set algorithm [23] performs curve regularization with a nonparametric median filter that reduces the computational cost, instead of using the curvature. Furthermore, it also replaces the numerical derivatives Δ^+ and Δ^- by the morphological erosion and dilation operations to induce curve propagation. Thus, the fast level set algorithm evolves according to the model

$$\psi_{\bar{r}}^{k+1} = \psi^k + \Delta t \times \left(\max(F,0) \cdot (\psi^k \oplus E)\ - \min(F,0) \cdot (\psi^k \ominus E)\right), \tag{4}$$

where $\oplus$ and $\ominus$ denote morphological dilation and erosion operations, respectively, with a disk-shaped structuring element E, and $\psi_{\bar{r}}$ refers to the non-regularized front. At each step of the hierarchical process, we used a disk of radius 1, as in [23], $\Delta t = 0.5$ according to [17], [23] and [38], and an initial level set function

or initial surface $\psi^{k=0}$ obtained by applying the algorithm presented in Section 3.2.

Finally, the front regularization is given by

$$\psi^{k+1} = \text{MedianFilt}\left[\psi_{\vec{r}}^{k+1}\right], \tag{5}$$

where the operator MedianFilt $[\cdot]$ is the median filter.

We performed statistical hypothesis tests with several distributions, and the image regions better fitted to a Gaussian distribution $f_{\mathcal{N}}(x;\mu,\sigma^2)$. Therefore, the binary median narrow band level set embodies a likelihood cost function defined in [24]

$$F = \log f_{\mathcal{N}}(x;\mu_1,\sigma_1^2)\vec{\eta} - \log f_{\mathcal{N}}(x;\mu_2,\sigma_2^2)\vec{\eta}, \tag{6}$$

where the parameters (μ_1,σ_1^2) and (μ_2,σ_2^2) are the mean and variance of the two detected clusters by applying the cluster detection algorithm in Section 3.2.

The median filter, embodied in our median narrow band level set implementation, is applied only to the narrow band for curve regularization. Similarly, the likelihood cost function F is only updated within the narrow band. Figure 2 shows a narrow band around the propagation curve of a user-defined width W_{NB}, that corresponds to the width, in pixels, from the curve to each narrow band boundary. As stated in [17], we used $W_{NB} = 3$ and when the front touches the edge of the narrow band, the calculation stops, and the algorithm builds a new narrow band with the front at the center.

Figure 2: Example of a narrow band (in white) around the propagation curve (in red).

3.2. Proposed Cluster Detection Algorithm for Level Set Initialization

Clustering algorithms commonly divide sample points into a predefined number of clusters. In Pap test images, it is not a trivial task to associate different cell structures, especially the nucleus, cytoplasm, and background to different clusters. In general, image regions are divided into more than three clusters to

generate satisfactory nucleus segmentation results. Therefore, the number of clusters is required a priori, which poses an additional challenge to cluster-based segmentation algorithms. Inspired by [39, 40], we propose an algorithm that overcomes these shortcomings and estimates the number of clusters and centroids according to the number of peaks in the histogram of the original cell image. Figure 3 exhibits the steps of the proposed cluster detection method.

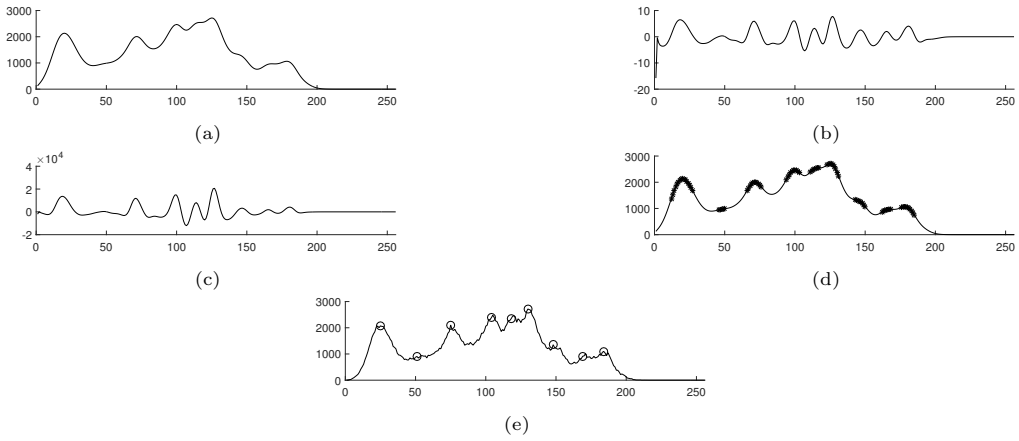

Figure 3: Cluster detection procedure: a) the smoothed image histogram (W_0); b) first level of the *à trous* wavelet detail coefficients (W_1); c) correlation signal ($corr_0$); d) detected clusters indicated by ($*$); and e) the original image histogram with points that represent the cluster centroids ($\circ$).

The algorithm performs a low-pass Gaussian filtering on the original image histogram and, then, it decomposes the smoothed histogram (W_0) (Figure 3a) and correlates W_0 with W_1 (Figure 3b), which is the first level of the *à trous* wavelet detail coefficients. The correlation signal ($corr_0$) (Figure 3c) is derived from the product between W_0 and W_1 according to [40]. The algorithm compares the correlation signal with the magnitude of the first level of wavelet detail coefficients. Furthermore, it maps the points that satisfy the condition $corr_0 > |W_1|$ [40] into the filtered histogram. Figure 3d displays points (marked with asterisks) in the histogram which represent clusters that support the estimation of centroids. We estimate these centroids in the original histogram by adopting the local maximum of each cluster. Figure 3e illustrates the centroids.

In this paper, we set the 1-D Gaussian filter bandwidth to $L = 6\sigma$, as suggested in [41], where σ is the standard deviation. Thus, the smoothing process can be defined as a scale-space representation, where σ is the scale parameter. The higher the σ value, the lower the number of clusters. Initially, we set $\sigma = 1$, and increase it, with step 1, until the algorithm detects only the two main clusters.

The fast level set algorithm [23], described in Section 3.1, requires an initial surface. This initialization consists of an image composed of two regions (background and foreground), where the boundary between the regions represents the propagation curve. In this paper, the initial surface is calculated by thresholding

the image histogram at the mid graylevel between the centroids of the two detected clusters, as depicted in Figure 4b. The region inside the curve consists of all pixels whose gray values are lesser than the threshold, whereas the outside region corresponds to its complement. This procedure to obtain the initial surface is used in the cellular mass segmentation stage and in the following steps of the hierarchical process. Figure 4c shows the initial surface which is the output image of the thresholding technique. In fact, this surface, which is close to the final segmentation result, leads the level set algorithm to converge within a few iterations. It is worth mentioning that, at each step of the hierarchical process, the histogram is calculated only in the current region as well as the thresholding technique is applied only to this currently analyzed region. For example, in the illustrations containing cells in Figure 1, the white regions are not considered in the current division.

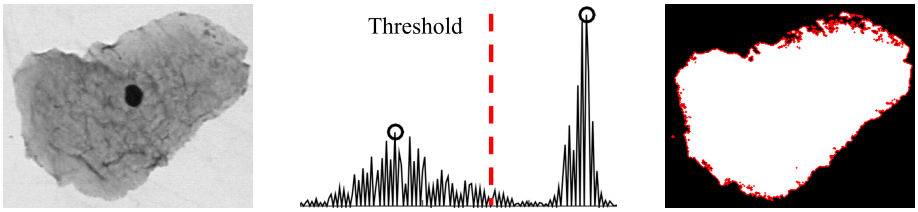

(a) Cell image. (b) Threshold and the two detected centroids (marked as ○). (c) Initial surface.

Figure 4: Obtaining the initial surface by image thresholding.

3.3. Proposed Hierarchical Level Set Implementation

To perform a multi-region segmentation, we introduce a hierarchical implementation based on the binary median narrow band level set for nuclei segmentation on Pap smear images. In fact, the cluster detection method embodied in the proposed segmentation algorithm promotes the hierarchical division. Thus, our segmentation algorithm only performs a new region division if the current region presents two or more clusters and, it stops when all regions cannot be further divided. The foreground (cellular mass) and background regions are obtained in the first step of the segmentation of the whole image. In most cases, the background and foreground regions are obtained in the first binary division. However, sometimes, cytoplasm parts with higher mean gray level are misclassified as background. Thus, after the first division, the background region is recursively divided by the median narrow band level set algorithm. The final segmentation result of the background is the region with the highest mean gray level. The final segmentation result of the cellular mass is the union of the possible segments obtained with the recursive segmentation of the background and the cellular mass obtained in the first division. The cellular mass segments are, individually, considered as new regions, and then they are partitioned into new ones, recursively. More specifically, for each cellular mass

segment, a bounding box is calculated as the minimum rectangle that contains the segment and then this region is, recursively, partitioned into new ones. The positions and sizes of the bounding boxes are saved and the identified nuclei are included in the final segmentation result in the corresponding position.

It is worth mentioning that although the main goal of the segmentation algorithm is to identify nuclei in cervical cells, background and cytoplasm segments can also be attainable during the hierarchical process. Thus, at each step of the hierarchical process, we compute features from each segment of the new regions such as size (S_n), circularity (C_n), minor and major axis ratio (AR_n), mean gray level (μ_n) and the difference between mean gray level and neighborhood gray level (D_n), since nuclei regions are smaller, darker and circular when compared to cytoplasm and background regions [5]. To assign a segment as nucleus, both in single cell and overlapping cells, the calculated features such as size must be between minimum and maximum values. The examples 1 and 2 in Figure 1 show the hierarchical divisions in a single cell and in overlapping cells, respectively, and the arrows indicate the segments identified as nucleus.

Since images from different databases have different resolutions, we used the minimum and maximum values in μm ($16.26 < S_n < 551.96$), inspired by [42]. Thus, given the image resolution (μm/pixels), we compute the corresponding values in pixels. The feature μ_n must be less than a maximum value ($\mu_n < 200$) as reported in [43] and D_n greater than a minimum disparity value ($D_n > 35$), which was obtained empirically. We achieved a higher number of correctly detected nuclei with the minimum value of disparity equal to 35 by varying it from 0 to 100, with an incremental step equal to 5. To ignore linear structures, the circularity must be greater than a minimum value ($C_n > 0.2$), as stated in [44], and the minor and major axis ratio must be greater than a minimum value ($AR_n > 0.3$), where this minimum value was obtained empirically. We eliminated a higher number of false nuclei with this minimum value by varying it from 0.1 to 1, with an incremental step equal to 0.1. In addition, we computed the area ratio between nucleus and cytoplasm (R_n), where a nucleus segment must also have ($R_n < 0.77$), in accordance with [42]. Thus, with the exception of the minimum and maximum values of the feature (S_n), which are calculated based on the image resolution, the same values for features (C_n), (AR_n), (μ_n), (D_n) and (R_n) were used in the segmentation experiments carried out on cervical cells of three image databases. In order to refine the segmentation results, each identified nucleus is considered a new region and, if it presents two or more clusters, a new partition is performed. One of the new regions obtained can also be identified as nucleus. In this case, the region with greater circularity is considered as nucleus, as Figure 5 illustrates.

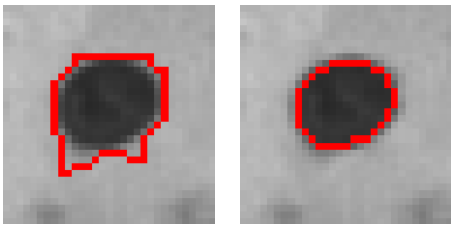

(a) (b)

Figure 5: Refinement of the nucleus segmentation result: (a) first identified nucleus; and (b) second identified nucleus, with greater circularity, obtained from the division of the nucleus in (a).

4. Experimental Results

For performance assessment of the hierarchical median narrow band level set algorithm (HMLS), we carried out segmentation experiments on three image databases which have ground truth images. The first database has 16 Extended Depth of Field (EDF) images (1024 x 1024 pixels) [6] and it comprises 645 cervical cells. The second one is the ISBI 2014 challenge data set [27] with synthetic cervical cytology images (512 x 512 pixels). It consists of 45 training images and 900 test images. The third one is the Herlev data set [28] which contains 917 images of single cervical cells organized into 7 classes: 1-superficial squamous, 2-intermediate squamous, 3-columnar, 4-mild dysplasia, 5-moderate dysplasia, 6-severe dysplasia and 7-carcinoma in situ. It is worth mentioning that despite the differences among the three image databases concerning resolution, contrast, imaging source, images with single cells and clump of cells with different degrees of overlap, real and synthetic images, we have used the same parameters in the proposed algorithm, i.e., the median narrow band level set with a disk of radius 1 [23], $\Delta t = 0.5$ [17], [23], [38] and a narrow band of width $W_{NB} = 3$ [17]. The experiments ran on a dual-core processor with 3.2 GHz and 8 GB RAM, using Matlab on a Windows operating system.

Here, we perform a quantitative evaluation of the nuclei segmentation and, based on the segmentation results, we compute shape and texture features for classification experiments and performance evaluation. The main reason for performing these experiments is to assess the accuracy and impact of the segmentation results on cell image classification using the Herlev database which contains the class labels for each image.

4.1. Evaluation measures

The quantitative analysis of the nuclei segmentation results is based on the reports in [5, 6], which state that the result is correct if at least τ percent of the detected object overlaps the ground truth and vice versa. Similarly to [6], we have adopted $\tau = 0.6$ as the overlap threshold. We have also computed the object-based

precision (PRE_O) and recall (REC_O) measures, respectively, as

$$\begin{aligned} PRE_O &= \frac{\text{N}^\circ \text{ of correctly detected objects}}{\text{N}^\circ \text{ of all segmented objects}}, \\ REC_O &= \frac{\text{N}^\circ \text{ of correctly detected objects}}{\text{N}^\circ \text{ of all objects in the ground truth}}. \end{aligned} \tag{7}$$

Likewise, the segmentation accuracy of each correctly detected nucleus is calculated in terms of pixel-based precision and recall according to [5]:

$$PRE_P = \frac{TP}{TP + FP}; \tag{8}$$

$$REC_P = \frac{TP}{TP + FN}, \tag{9}$$

where TP (true-positive) is the number of correctly segmented pixels, FP (false-positive) is the number of segmented pixels that are not in the ground truth and FN (false-negative) is the number of pixels in the ground truth that are not in the segmentation result.

We have also applied the Dice similarity coefficient (DSC) or Zijdenbos similarity index [45] to measure the segmentation accuracy, which is defined as

$$DSC = 2\frac{\#\{O_{GT} \cap O_{SR}\}}{\#\{O_{GT}\} + \#\{O_{SR}\}} = \frac{2TP}{2TP + FP + FN}, \tag{10}$$

where O_{GT} denotes the ground truth region, O_{SR} the segmented region, and $\#\{\cdot\}$ the number of pixels in a region. DSC values greater than 0.7 indicate an adequate matching between the ground truth and segmented regions [45].

To evaluate the classification results, we have followed the methodology introduced in [8]. Thus, we have computed the precision or positive predictive value (PPV), sensitivity ($SENS$), specificity (SPE), F-score (FS) and accuracy (ACC) measures, respectively, as defined in [46]:

$$PPV = \frac{\sum_{i=1}^{N} \frac{tp_i}{tp_i + fp_i}}{N}; \tag{11}$$

$$SENS = \frac{\sum_{i=1}^{N} \frac{tp_i}{tp_i + fn_i}}{N}; \tag{12}$$

$$SPE = \frac{\sum_{i=1}^{N} \frac{tn_i}{tn_i + fp_i}}{N}; \tag{13}$$

$$FS = 2\frac{PPV * SENS}{PPV + SENS}; \tag{14}$$

$$ACC = \frac{\sum_{i=1}^{N} \frac{tp_i + tn_i}{tp_i + tn_i + fp_i + fn_i}}{N}, \tag{15}$$

where tp_i (true-positive) is the number of correctly recognized examples of class C_i, tn_i (true-negative) is the number of correctly recognized examples that do not belong to the class C_i, fp_i (false-positive) is the number of examples that either were incorrectly assigned to the class C_i, fn_i (false-negative) is the number of examples that were not recognized as class C_i and N denotes the number of classes.

4.2. Segmentation experiment 1: EDF images and ISBI 2014 challenge data set

We carried out experiments on the 16 EDF images and 900 test images of the ISBI 2014 challenge data set to evaluate the HMLS. Both data sets contain overlapping cells which also pose difficulties for nuclei segmentation. Moreover, we compared our method to MSERLS [6] and LTSN [29] on the 16 EDF images. In addition to these two methods, we also compared it to DeepCNN1 [3] on the test images of the ISBI 2014 challenge data set, where the values of the evaluation measures are reported in [3]. The training step of DeepCNN1 was conducted on the 45 training images of the ISBI 2014 challenge data set, each with 441 patches. The publicly available code in [6], implemented in Matlab, was used to run MSERLS. Here, we applied the code provided by Ushizima *et al.* [29] to run the segmentation method in [29], implemented using Fiji. Figure 6 illustrates EDF images and test images of the ISBI 2014 challenge data set.

Table 1 shows the evaluation metrics of the experiments performed on 16 EDF images. Concerning the object-based nuclei detection, our method outperformed MSERLS and LTSN in terms of PRE_O and REC_O measures. The good results achieved by HMLS were due to the higher number of correctly segmented nuclei and the smaller number of false nuclei. Our pixel-based results were evaluated in terms of PRE_P, REC_P and DSC. Despite obtaining the lowest precision value, our method achieved the higher recall and DSC values in comparison with the results of the method introduced in [29] and similar to the ones obtained in [6]. Regarding the mean computation time, our algorithm and the ones proposed in [6] and [29] achieved 28.62 s, 36.56 s and 3 s, respectively.

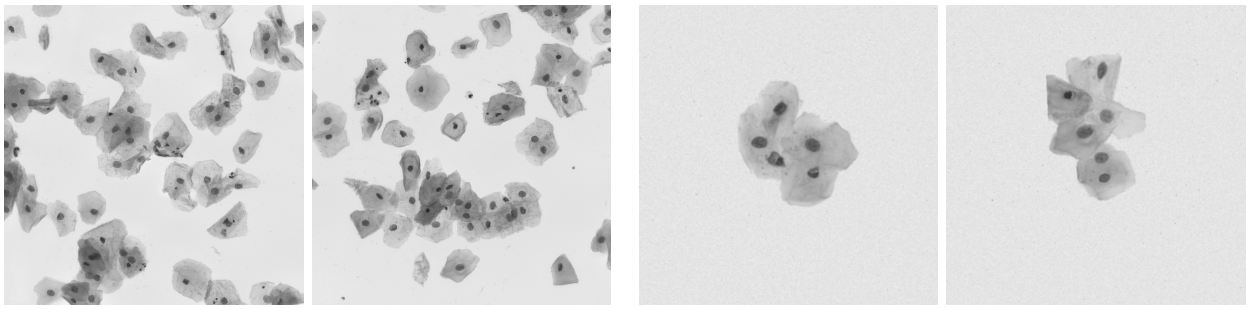

(a) (b)

Figure 6: Cervical cell images: (a) EDF images (1024 x 1024) and (b) test images (512 x 512) of the ISBI 2014 challenge data set.

Table 1: Comparison of nuclei segmentation results of the 16 EDF images.

Algorithm	PRE_O	REC_O	PRE_P	REC_P	DSC
HMLS	0.81	0.86	0.95 ± 0.07	0.90 ± 0.08	0.92 ± 0.05
MSERLS	0.73	0.85	0.96 ± 0.06	0.90 ± 0.08	0.92 ± 0.05
LTSN	0.72	0.79	0.97 ± 0.05	0.86 ± 0.09	0.91 ± 0.05

Table 2 presents the evaluation metrics of the segmentation results on the test images of the ISBI 2014 challenge data set. Concerning the object-based nuclei detection, despite the lowest precision value PRE_O, our method outperformed MSERLS, LTSN and DeepCNN1 in terms of the REC_O measure. In pixel-based evaluation, HMLS achieved higher recall and DSC values than the LTSN method and higher recall and similar DSC values to MSERLS, despite the high precision values of MSERLS and LTSN methods. The best results were obtained by DeepCNN1 and our results achieved values comparable to this method. With respect to the mean computation cost, HMLS, MSERLS, LTSN obtained 3 s, 8.10 s and 1.98 s, respectively. Tareef *et al.* [3] reported that the DeepCNN1 algorithm spent 8 s running on a computer with Intel Core i5 3.2 GHz and 8 GB RAM [3]. The configuration of this computer is similar to the one used to run our experiments.

Table 2: Comparison of nuclei segmentation on the ISBI 2014 data set.

Algorithm	PRE_O	REC_O	PRE_P	REC_P	DSC
HMLS	0.95	0.93	0.93 ± 0.08	0.93 ± 0.07	0.92 ± 0.04
MSERLS	0.98	0.88	0.94 ± 0.08	0.91 ± 0.08	0.92 ± 0.05
LTSN	0.96	0.90	0.97 ± 0.06	0.87 ± 0.07	0.91 ± 0.04
DeepCNN1	0.99	0.91	0.94 ± 0.06	0.95 ± 0.06	0.94 ± 0.04

4.3. Segmentation experiment 2: the Herlev data set

We carried out this experiment on individual cell images to evaluate our method and compare it to RGVF [30], MFCM [31] and DeepCNN2 [32], which were designed for single cell image segmentation and applied to the Herlev database in these original articles. The publicly available code in [30], implemented in Matlab, was used to run RGVF while to MFCM, we applied a 7×7 median filter on grayscale image and used the Matlab function *fcm*, with its standard parameters, to divide the filtered image into 7 clusters based on the gray levels. Each cluster is represented by its value of center (mean gray level) and the clusters whose values of center are less than the nucleus threshold (80% of the mean of cluster centers) are considered as nucleus. The clusters with the values of center between the nucleus threshold and cytoplasm threshold (120% of the mean of cluster centers) are considered as cytoplasm. The remaining clusters are considered as background. Finally, morphological operations, i.e., opening and closing, were applied successively (10 iterations) with a disk-shaped structuring element with 7-pixel radius according to [31]. In addition, we also compared our method to DeepCNN2 [32], where the values of the pixel-based evaluation measures were obtained directly in [32]. It is worth noting that the authors in [32] did not conduct an object-based assessment.

HMLS accomplished a higher number of correctly detected nuclei for classes 1, 2, 3 and 7. Table 3 summarizes these results. It is worth mentioning that nuclei detection is a crucial task for other processing steps such as feature extraction and classification. Table 4 presents the pixel-based evaluation metrics of the experiments performed on images from the Herlev data set and the bold values point out the best average results. In accordance with these results, our method accomplished high average precision and DSC values, despite the high average recall value of RGVF algorithm. In fact, the hierarchical method succeeded due to the higher number of correctly segmented pixels (TP). Nevertheless, the RGVF algorithm presented lower values of false-negative (FN). Figure 7 shows the results on images from the Herlev database. Regarding the mean computation time, HMLS, RGVF and MFCM spent 0.99 s, 11.41 s and 1.62 s, respectively.

Table 5 presents the quantitative comparison of the segmentation results obtained by the proposed method and DeepCNN2 in terms of PRE_P, REC_P and DSC computed from the segmentation results of all images, as in [32]. HMLS achieved higher average PRE_P and REC_P values and similar average DSC value.

4.4. Classification experiment

We performed classification experiments on images from the Herlev database since it contains annotated images, each one with a manually segmented version that can be used as ground-truth. The inputs of the

Table 3: Number of correctly detected nuclei on the Herlev data set.

Class	Class name	Class size	Algorithm		
			HMLS	RGVF	MFCM
1	Superficial squamous	74	73	57	58
2	Intermediate squamous	70	70	53	64
3	Columnar	98	84	81	70
4	Mild dysplasia	182	153	156	127
5	Moderate dysplasia	146	127	135	105
6	Severe dysplasia	197	178	182	143
7	Carcinoma in situ	150	138	134	92
	Total	917	823	798	659

Table 4: Comparison of nuclei segmentation results on the Herlev data set. The pixel-based measures were calculated from the correctly detected nucleus for $\tau = 0.6$ and the classes are numbered as in Table 3.

Class		*Precision* (PRE_P)			*Recall* (REC_P)			*DSC*		
		HMLS	RGVF	MFCM	HMLS	RGVF	MFCM	HMLS	RGVF	MFCM
1	μ	0.87	0.87	0.89	0.98	0.98	0.96	0.92	0.92	0.92
	σ	0.10	0.09	0.12	0.05	0.02	0.06	0.05	0.05	0.06
2	μ	0.91	0.88	0.92	0.98	0.99	0.97	0.94	0.93	0.94
	σ	0.07	0.06	0.09	0.04	0.01	0.04	0.04	0.03	0.04
3	μ	0.92	0.83	0.89	0.94	0.98	0.91	0.92	0.90	0.89
	σ	0.10	0.09	0.11	0.08	0.02	0.10	0.06	0.06	0.07
4	μ	0.96	0.90	0.95	0.95	0.99	0.92	0.95	0.94	0.93
	σ	0.07	0.08	0.08	0.08	0.04	0.10	0.05	0.05	0.07
5	μ	0.96	0.89	0.94	0.93	0.97	0.90	0.94	0.93	0.91
	σ	0.08	0.09	0.10	0.08	0.06	0.12	0.06	0.06	0.07
6	μ	0.96	0.91	0.95	0.93	0.96	0.89	0.94	0.93	0.91
	σ	0.07	0.08	0.09	0.08	0.06	0.10	0.05	0.05	0.06
7	μ	0.93	0.91	0.94	0.93	0.94	0.85	0.92	0.92	0.88
	σ	0.10	0.08	0.09	0.08	0.08	0.12	0.06	0.06	0.08
Average	μ	**0.93**	0.88	**0.93**	0.95	**0.97**	0.92	**0.93**	0.92	0.91
	σ	0.08	0.08	0.10	0.07	0.04	0.09	0.05	0.05	0.06

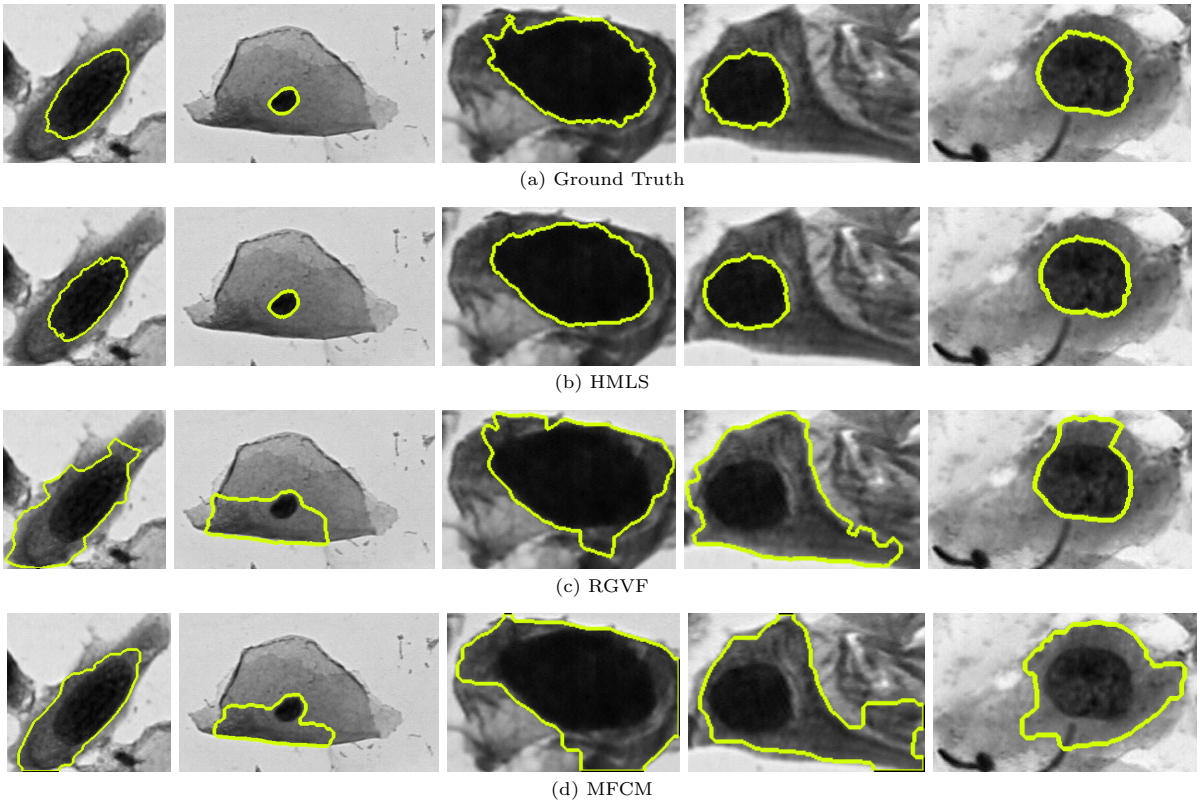

(a) Ground Truth

(b) HMLS

(c) RGVF

(d) MFCM

Figure 7: Cell images from Herlev data set, the Ground truth and the segmentation results for each method. (a) Ground truth of cell nuclei, (b) HMLS, (c)RGVF and (d) MFCM.

Table 5: Comparison of nuclei segmentation on the Herlev data set. The pixel-based measures were calculated from the segmentation results of all images and the classes are numbered as in Table 3.

Class		*Precision* (PRE_P)		*Recall* (REC_P)		*DSC*	
		HMLS	DeepCNN2	HMLS	DeepCNN2	HMLS	DeepCNN2
1	μ	0.87	0.94	0.98	0.79	0.92	–
	σ	0.11	–	0.05	–	0.06	–
2	μ	0.91	0.90	0.98	0.92	0.94	–
	σ	0.07	–	0.04	–	0.04	–
3	μ	0.87	0.87	0.92	0.91	0.88	–
	σ	0.17	–	0.14	–	0.14	–
4	μ	0.93	0.87	0.91	0.97	0.89	–
	σ	0.14	–	0.20	–	0.19	–
5	μ	0.94	0.93	0.89	0.96	0.89	–
	σ	0.12	–	0.20	–	0.18	–
6	μ	0.94	0.78	0.92	0.97	0.92	–
	σ	0.11	–	0.12	–	0.11	–
7	μ	0.90	0.92	0.90	0.87	0.89	–
	σ	0.17	–	0.17	–	0.15	–
Average	μ	**0.91**	0.89	**0.93**	0.91	**0.90**	**0.90**
	σ	0.13	–	0.13	–	0.12	–

classification algorithms are features based on shape and texture, as in [8]. From the segmentation results, we have extracted 5 shape features from the nucleus, namely, area, perimeter, eccentricity, compactness, and circularity which compose the vector f_{Shape}. Thus, we generated the vector f_{Shape} for the ground truth nucleus (GT) and the corresponding segmentation results obtained from HMLS, RGVF, and MFCM. Additionally, we extracted 6 texture features by using the first order statistics of the histogram, namely, mean, variance, kurtosis, skewness, energy, and entropy which comprise the vector $f_{Histogram}$.

Then, the algorithms Least Square Support Vector Machine (LSSVM) [47] (with a radial basis function kernel), Multilayer Perceptron (MLP) [48] (with 4 hidden layers, logistic activation function and trained using the back-propagation algorithm) and Random Forest (RF) [49] (with 60 bags to use for boostrapping) classified the cervical cells into two and three classes, based on the 11 features $f_{Final} = \{f_{Shape}, f_{Histogram}\}$. For three-class classification experiment, we have divided data into normal (superficial squamous, intermediate squamous and columnar), LSIL (mild dysplasia), and HSIL (moderate dysplasia, severe dysplasia and carcinoma in situ) classes in accordance with the Bethesda system, which is used for diagnosis of precancerous and cancerous cervical cells. For two-class classification experiment, the last two classes (LSIL and HSIL) were joined and named as an abnormal class. To compute the average values of the classification

measures, we carried out 100 executions and for each execution, we have partitioned the data set randomly into two independent subsets, i.e., the test set with 30% of data and the training set with 70% of data.

Table 6 shows the evaluation measures for the two-class classification results and Table 7 presents the evaluation measures for the three-class classification experiment. The italic values point out the results achieved by the classifiers LSSVM, MLP and RF using the ground truth nucleus. In this paper, we have assumed these results as a reference for comparison and performance evaluation. The bold values indicate the best results for each measure and they correspond to the closest results to those obtained with the ground truth nucleus.

Table 6: Comparison of classification results on the Herlev data set to 2 classes (normal and abnormal).

Methods		*SPE*	*SENS*	*PPV*	*FS*	*ACC*
LSSVM	GT	*0.93±0.02*	*0.93±0.01*	*0.94±0.01*	*0.93±0.01*	*0.93±0.01*
	HMLS	**0.89±0.04**	**0.89±0.02**	**0.91±0.02**	**0.90±0.02**	**0.89±0.02**
	RGVF	0.86±0.05	0.87±0.02	0.90±0.02	0.88±0.02	0.87±0.02
	MFCM	0.85±0.05	0.86±0.02	0.89±0.02	0.87±0.02	0.86±0.02
MLP	GT	*0.92±0.03*	*0.93±0.01*	*0.94±0.01*	*0.94±0.01*	*0.93±0.01*
	HMLS	**0.86±0.05**	**0.89±0.02**	**0.90±0.02**	**0.89±0.02**	**0.89±0.02**
	RGVF	0.83±0.05	0.84±0.02	0.89±0.02	0.85±0.02	0.84±0.02
	MFCM	0.82±0.05	0.85±0.01	0.88±0.02	0.86±0.01	0.85±0.01
RF	GT	*0.90±0.03*	*0.93±0.01*	*0.93±0.01*	*0.93±0.01*	*0.93±0.01*
	HMLS	**0.87±0.04**	**0.89±0.02**	**0.90±0.02**	**0.90±0.02**	**0.89±0.02**
	RGVF	0.82±0.04	0.87±0.02	0.88±0.02	0.87±0.02	0.87±0.02
	MFCM	0.83±0.04	0.86±0.02	0.89±0.02	0.87±0.02	0.86±0.02

Table 7: Comparison of classification results on the Herlev data set to 3 classes (normal, LSIL and HSIL).

Methods		*SPE*	*SENS*	*PPV*	*FS*	*ACC*
LSSVM	GT	*0.89±0.04*	*0.80±0.04*	*0.84±0.04*	*0.81±0.04*	*0.80±0.04*
	HMLS	**0.87±0.01**	**0.85±0.01**	**0.85±0.01**	**0.84±0.01**	**0.77±0.01**
	RGVF	0.82±0.05	0.73±0.03	0.75±0.04	0.73±0.03	0.73±0.03
	MFCM	0.83±0.02	0.73±0.02	0.77±0.03	0.74±0.01	0.73±0.02
MLP	GT	*0.84±0.02*	*0.77±0.02*	*0.79±0.02*	*0.78±0.02*	*0.77±0.02*
	HMLS	**0.81±0.03**	**0.73±0.03**	**0.76±0.03**	**0.74±0.03**	**0.73±0.03**
	RGVF	0.78±0.04	0.68±0.04	0.74±0.03	0.70±0.03	0.68±0.04
	MFCM	0.80±0.05	0.70±0.04	0.75±0.04	0.72±0.04	0.70±0.04
RF	GT	*0.85±0.02*	*0.79±0.02*	*0.80±0.02*	*0.79±0.02*	*0.79±0.02*
	HMLS	**0.84±0.02**	**0.76±0.02**	**0.79±0.02**	**0.77±0.02**	**0.76±0.02**
	RGVF	0.82±0.02	0.74±0.02	0.76±0.02	0.75±0.02	0.74±0.02
	MFCM	0.81±0.03	0.73±0.02	0.76±0.02	0.74±0.02	0.73±0.02

In addition, we provided the ROC curves and the area under the curve (AUC) for the classification

experiments with two classes, where the x axis represents the false positive rate (1-specificity) and the y axis represents the true positive rate (sensitivity). Figure 8 shows the ROC curves of the classification experiments using features extracted from the ground truth (Figure 8(a)) and segmentation results of cell nuclei.

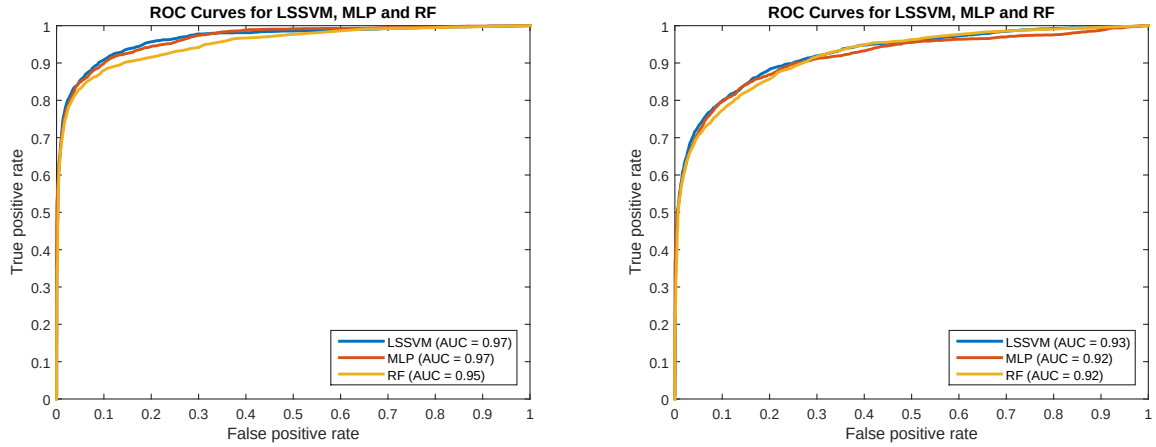

(a) Ground truth.

(b) HMLS.

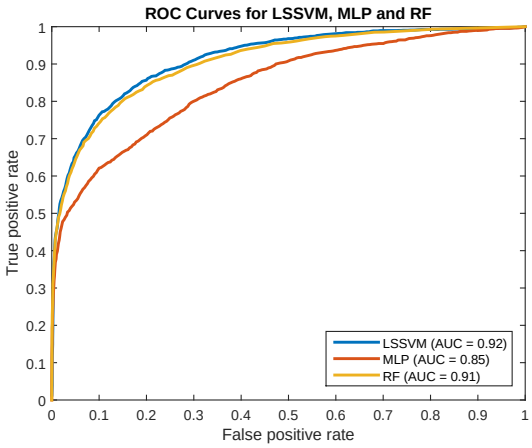

(c) RGVF

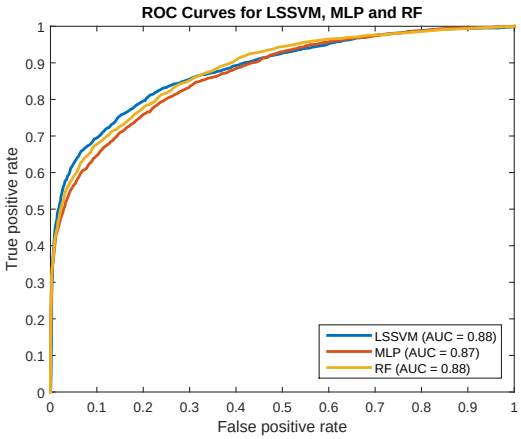

(d) MFCM

Figure 8: ROC curves and AUC of each method for two-class classification experiments using features extracted from the (a) Ground truth images and (b) HMLS, (c) RGVF and (d) MFCM image segmentation results.

5. Discussion

Experiments with the 16 EDF images are summarized in Table 1 and indicate more accurate segmentation results, in terms of PRE_O and REC_O, when using HMLS due to the higher number of correctly segmented nuclei and smaller number of false nuclei. HMLS was more efficient in regions with low mean gray level difference between nucleus and cytoplasm that can occur due to inconsistent staining, poor contrast or

overlapping cells. These results showed the robustness of the proposed segmentation method to low contrast cell images and overlapping cell images with different degrees of overlap. HMLS obtained higher values of REC_P and DSC compared to LTSN and similar to MSERLS while the LTSN method achieved the higher value of PRE_P. This was due to the higher number of correctly segmented pixels (TP) obtained by HMLS and MSERLS algorithms and lower value of false-positive (FP) obtained by LTSN.

Table 2 shows the comparison of nuclei segmentation results on the test images of the ISBI 2014 challenge data set. Due to the higher number of correctly segmented nuclei obtained by HMLS, it outperformed MSERLS, LTSN and DeepCNN1 in terms of the REC_O measure, despite the lowest precision value PRE_O. A high REC_O value, indicating high true positive rate, is more important than high PRE_O since each nucleus can represent a cell in a possible next step for cytoplasm segmentation. For example, the methods in [3, 6, 29] use the nucleus information to then obtain the cytoplasm. Concerning the pixel-based evaluation, HMLS achieved higher or similar values of REC_P and DSC compared to MSERLS and LTSN methods, although it has obtained the lowest value of PRE_P, and results comparable with DeepCNN1. As mentioned in Section 2, DeepCNN1 first splits an image into fixed-size patches, and then it performs CNN-based feature learning and classification on the patches to identify nuclei, cellular mass, and background. To generate image patches, DeepCNN1 uses the SLIC algorithm [37], where its parameter setting (S and r) is very important and have to be carefully tuned to get the best results. Thus, different values of S (superpixel size) and r (shape regularity) may be required for different data sets. In [3], the S and r parameters were set empirically to 25 and 0.01, respectively. An advantage of our cervical cell nucleus segmentation method is that it can be applied to different data sets without requiring a training stage.

Table 3 presents the segmentation results of the Herlev data set, and our proposal detected a higher number of nuclei for most classes. The image results in Figure 7 demonstrated that RGVF and MFCM achieve less accurate segmentation results on images with more than three clusters and when nucleus, cytoplasm, and background were poorly defined. It is worth noting that cytoplasm areas with low intensity tend to be misclassified as nuclei. In addition, these misclassified results may be related to the limit of 3 classes imposed by RGVF and MFCM to the image regions. Differently, HMLS did not require prior knowledge about the number of clusters and did not specify a fixed number of them. For each new region, it searched for two new clusters. Table 5 presents the nuclei segmentation results obtained by HMLS and DeepCNN2, where HMLS accomplished similar average DSC value and higher average PRE_P and REC_P values. HMLS succeeded due to the higher number of correctly segmented pixels (TP).

The results in Tables 1–5 demonstrated that the proposed hierarchical method is capable of satisfactorily

segmenting cell nucleus in multiple overlapping cell images as well as in single cell images. In Section 3.3, we mentioned that the nucleus identification process consists in applying thresholds to six features extracted from the segmented regions. Each identified nucleus is subjected to a refinement process, in which the circularity feature is used to obtain the most likely object to be nucleus. However, sometimes the identified nucleus corresponds to chromatin regions or darker regions within the nucleus, due to overlapping cells, cell fragments, etc. This is a shortcoming of our algorithm that should be overcome.

According to the average values of PPV, $SENS$, SPE, FS and ACC measures in Table 6 and Table 7, the proposed hierarchical method for nuclei segmentation outperformed the others for both two-class and three-class classification experiments using the features extracted from our segmentation results. We achieved classification results which are the closest ones to those obtained with the ground truth nuclei. The better performance of the three classification algorithms in Figure 8(b), when comparing to Figure 8(c) and Figure 8(d), may be due to nucleus shape and texture features well preserved in the cell images processed by HMLS. We can affirm that the proposed algorithm was able to preserve subtle details of nuclei shapes, regardless image differences in resolution, contrast or texture. Overall, our segmentation results have improved the classification of cell images into normal and abnormal. Figure 8(b) confirms that our method improved simultaneously the performance of the three classification algorithms when comparing it to the ROC curves obtained with features extracted from the ground truth of cell nuclei in Figure 8(a). These experiments demonstrated that classification experiments, driven by nuclei features, to recognize normal and abnormal patterns of cervical cells benefit from accurate cell nuclei segmentation algorithms.

6. Conclusion

Automatic nuclei segmentation is a suitable task to reduce analysis time as well as expertise dependency and integrate decision support systems for cervical cell screening and early detection of cervical cancer. Here, we propose a hierarchical narrow band level set algorithm for nuclei segmentation that is a crucial step to perform cervical cell classification experiments that rely on nuclei shape and texture features. The proposed hierarchical segmentation algorithm does not rely on prior information about the number of image clusters. In fact, the reliance upon a predefined number of cluster hinders the ability of cell image segmentation algorithms to achieve accurate results and to deal with different image databases. Our segmentation algorithm embodies a new cluster detection strategy that guides the hierarchical process. This strategy is used to initialize the median narrow band level set algorithm which is the core of our algorithm. The proposed method is able to segment cells of low contrast more efficiently within this hierarchical approach. This is

mainly due to the sensitivity of the cluster detection method to subtle graylevel differences when applied to the smaller image regions that appear later in the recursive partitioning. Our experiments comprised three cell image databases which are challenging and present remarkable differences concerning resolution, contrast, imaging source, images with single cells and clump of cells with different degrees of overlap, real and synthetic images, to name a few. We evaluated six state-of-the-art cervical cell segmentation algorithms and the proposed hierarchical segmentation method was capable of identifying nucleus in single cell images as well as in multiple overlapping cell images, accurately. We also assessed the proposed segmentation algorithm by performing classification experiments, driven by nuclei features, to recognize normal and abnormal patterns of cervical cells considering differences in shape and chromatin distribution. The performance of the classification algorithms improved by using image features extracted from our nuclei segmentation results and, thus, they accomplished the smallest number of false negatives and the highest average accuracy values for two-class and three-class problems. In fact, our segmentation results provided a set of features quite similar to the ones extracted from the ground truth images that led us to conclude that it preserved intrinsic shape and texture differences among normal and abnormal cells.

Further work will extend and apply the hierarchical segmentation algorithm to other types of cell images. We will also approach both cell image segmentation and classification based on nuclei features of overlapping cervical cells from conventional Pap test with several overlapping cervical cells. Future investigations will also consider convolutional neural networks as part of schemes for real cell detection and classification.

Acknowledgements

This work was supported by Coordination for the Improvement of Higher Education Personnel - Finance Code 001 (CAPES) and National Council for Scientific and Technological Development (CNPq).

References

[1] I. Lowy, A Woman's Disease: The history of cervical cancer, 1st edition ed., Oxford University Press, New York, 2011.

[2] World Health Organization, Comprehensive cervical cancer control: a guide to essential practice, 2 ed., World Health Organization Press, 2014.

[3] A. Tareef, Y. Song, H. Huang, Y. Wang, D. Feng, M. Chen, W. Cai, Optimizing the cervix cytological examination based on deep learning and dynamic shape modeling, Neurocomputing 248 (2017) 28–40.

[4] A. Gertych, A. O. Joseph, A. E. Walts, S. Bose, Automated detection of dual p16/ki67 nuclear immunoreactivity in liquid-based Pap tests for improved cervical cancer risk stratification, Annals of Biomedical Engineering 40 (2012) 1192–1204.

[5] A. Gençtav, S. Aksoy, S. Önder, Unsupervised segmentation and classification of cervical cell images, Pattern Recognition 45 (2012) 4151–4168.

[6] Z. Lu, G. Carneiro, A. Bradley, An improved joint optimization of multiple level set functions for the segmentation of overlapping cervical cells, IEEE Transactions on Image Processing 24 (2015) 1261–1272.

[7] Z. Lu, G. Carneiro, A. P. Bradley, D. Ushizima, M. S. Nosrati, A. G. Bianchi, C. M. Carneiro, G. Hamarneh, Evaluation of three algorithms for the segmentation of overlapping cervical cells, IEEE Journal of Biomedical and Health Informatics 21 (2017) 441–450.

[8] K. Bora, M. Chowdhury, L. B. Mahanta, M. K. Kundu, A. K. Das, Automated classification of Pap smear images to detect cervical dysplasia, Computer Methods and Programs in Biomedicine 138 (2017) 31–47.

[9] D. Gupta, J. Arora, U. Agrawal, A. Khanna, V. H. C. de Albuquerque, Optimized binary bat algorithm for classification of white blood cells, Measurement 143 (2019) 180–190.

[10] M. E. Plissiti, C. Nikou, A. Charchanti, Combining shape, texture and intensity features for cell nuclei extraction in Pap smear images, Pattern Recognition Letters 32 (2011) 838–853.

[11] J. R. Tang, N. A. M. Isa, E. S. Ch'ng, A fuzzy-c-means-clustering approach: Quantifying chromatin pattern of non-neoplastic cervical squamous cells, PloS ONE 10 (2015) 1–15.

[12] S. Watanabe, T. Iwasaka, M. Yokoyama, M. Uchiyama, T. Kaku, T. Matsuyama, Analysis of nuclear chromatin distribution in cervical glandular abnormalities, Acta Cytologica 48 (2004) 505–513.

[13] B. Nielsen, F. Albregtsen, H. E. Danielsen, Statistical nuclear texture analysis in cancer research: a review of methods and applications, Critical Reviews™ in Oncogenesis 14 (2008) 89–164.

[14] M. E. Plissiti, C. Nikou, A. Charchanti, Automated detection of cell nuclei in Pap smear images using morphological reconstruction and clustering, IEEE Transactions on Information Technology in Biomedicine 15 (2011) 233–241.

[15] P. H. C. Oliveira, G. Moreira, D. M. Ushizima, C. M. Carneiro, F. N. S. de Medeiros, F. H. D. de Araújo, R. R. V. e Silva, A. G. C. Bianchi, A multi-objective approach for calibration and detection of cervical cells nuclei, in: 2017 IEEE Congress on Evolutionary Computation, CEC 2017, Donostia, San Sebastián, Spain, June 5-8, 2017, 2017, pp. 2321–2327. URL: https://doi.org/10.1109/CEC.2017.7969586. doi:10.1109/CEC.2017.7969586.

[16] Radial feature descriptors for cell classification and recommendation, Journal of Visual Communication and Image Representation 62 (2019) 105–116.

[17] J. A. Sethian, Level Set Methods and Fast Merging Methods: Evolving Interfaces in Computational Geometry, Fluid Mechanics, Comput. Vision and Materials Science, 1 ed., Cambridge University Press, Cambridge, 1999.

[18] E. S. Reboucas, A. M. Braga, R. C. Marques, P. P. Reboucas Filho, A new approach to calculate the nodule density of ductile cast iron graphite using a level set, Measurement 89 (2016) 316–321.

[19] A. Alarifi, A. Alwadain, Computer-aided cancer classification system using a hybrid level-set image segmentation, Measurement 148 (2019) 106864.

[20] Y. Wu, C. He, A convex variational level set model for image segmentation, Signal Processing 106 (2015) 123–133.

[21] Y. Liu, C. He, P. Gao, Y. Wu, Z. Ren, A binary level set variational model with L^1 data term for image segmentation, Signal Processing 155 (2019) 193–201.

[22] D. M. Ushizima, F. N. S. Medeiros, J. Cuadros, C. I. O. Martins, Vessel network detection using contour evolution and color components, in: 32nd Annual International Conference of the IEEE Engineering in Medicine and Biology, 2010, pp. 3129–3132.

[23] A. M. Braga, R. C. P. Marques, F. A. A. Rodrigues, F. N. S. Medeiros, A median regularized level set for hierarchical segmentation of SAR images, IEEE Geoscience and Remote Sensing Letters 14 (2017) 1171–1175.

[24] A. Mitiche, I. B. Ayed, Variational and Level Set Methods in Image Segmentation, volume 5, Springer-Verlag, Berlin, 2010.

[25] M. Jeon, M. Alexander, W. Pedrycz, N. Pizzi, Unsupervised hierarchical image segmentation with level set and additive operator splitting, Pattern Recognition Letters 26 (2005) 1461–1469.

[26] K. Ni, B.-W. Hong, S. Soatto, T. Chan, Unsupervised multiphase segmentation: A recursive approach, Computer Vision and Image Understanding 113 (2009) 502–510.

[27] Overlapping cervical cytology image segmentation challenge - ISBI 2014, 2014. URL: `https://cs.adelaide.edu.au/~carneiro/isbi14_challenge/`.

[28] J. Jantzen, G. Dounias, Analysis of Pap-smear image data, in: Nature-Inspired Smart Information Systems 2nd Annual Symposium, Tenerife, Spain, 2006, pp. 1–10.

[29] D. Ushizima, A. Bianchi, C. Carneiro, Segmentation of subcellular compartments combining superpixel representation with Voronoi diagrams, IEEE International Symposium on Biomedical Imaging (ISBI) (2014).

[30] K. Li, Z. Lu, W. Liu, J. Yin, Cytoplasm and nucleus segmentation in cervical smear images using Radiating GVF Snake, Pattern Recognition 45 (2012) 1255–1264.

[31] T. Chankong, N. Theera-Umpon, S. Auephanwiriyakul, Automatic cervical cell segmentation and classification in Pap smears, Computer Methods and Programs in Biomedicine 113 (2014) 539–556.

[32] S. Gautam, A. Bhavsar, A. K. Sao, K. Harinarayan, CNN based segmentation of nuclei in PAP-smear images with selective pre-processing, in: Medical Imaging 2018: Digital Pathology, volume 10581, International Society for Optics and Photonics, 2018, pp. 1–9.

[33] Y. Song, L. Zhang, S. Chen, D. Ni, B. Lei, T. Wang, Accurate segmentation of cervical cytoplasm and nuclei based on multiscale convolutional network and graph partitioning, IEEE Transactions on Biomedical Engineering 62 (2015) 2421–2433.

[34] J. Zhang, Z. Liu, B. Du, J. He, G. Li, D. Chen, Binary tree-like network with two-path fusion attention feature for cervical cell nucleus segmentation, Computers in Biology and Medicine 108 (2019) 223–233.

[35] T. Wan, S. Xu, C. Sang, Y. Jin, Z. Qin, Accurate segmentation of overlapping cells in cervical cytology with deep convolutional neural networks, Neurocomputing 365 (2019) 157–170.

[36] K. H. S. Allehaibi, L. E. Nugroho, L. Lazuardi, A. S. Prabuwono, T. Mantoro, et al., Segmentation and classification of cervical cells using deep learning, IEEE Access 7 (2019) 116925–116941.

[37] H. Shah-hosseini, SLIC superpixels compared to state-of-the-art superpixel methods, IEEE Trans. Pattern Anal. Mach. Intell 24 (2002) 1388–1393.

[38] K. Zhang, H. Song, L. Zhang, Active contours driven by local image fitting energy, Pattern Recognition 43 (2010) 1199–1206.

[39] G. Sita, A. G. Ramakrishnan, Wavelet domain nonlinear filtering for evoked potential signal enhancement, Computers and Biomedical Research 33 (2000) 431–446.

[40] I. C. Paula Jr, F. N. S. Medeiros, F. N. Bezerra, D. M. Ushizima, Multiscale corner detection in planar shapes, Journal of Mathematical Imaging and Vision 45 (2012) 251–263.

[41] R. C. Gonzalez, R. E. Woods, Digital Image Processing, 2 ed., Prentice Hall, New Jersey, 2002.

[42] M. Wesoła, A. Lipiński, M. Jeleń, Morphometry in the cytological diagnosis of cervical smears., Advances in clinical and experimental medicine: official organ Wroclaw Medical University 23 (2014) 289–293.

[43] N. A. Mat-Isa, M. Y. Mashor, N. H. Othman, An automated cervical pre-cancerous diagnostic system, Artificial Intelligence in Medicine 42 (2008) 1–11.

[44] V. Raghavan, K. R. Rao, An imagej based semi-automated morphometric assessment of nuclei in oncopathology, International Journal of Scientific Study 3 (2015) 189–194.

[45] A. P. Zijdenbos, B. M. Dawant, R. A. Margolin, A. C. Palmer, Morphometric analysis of white matter lesions in MR images: method and validation, IEEE Transactions on Medical Imaging 13 (1994) 716–724.

[46] M. Sokolova, G. Lapalme, A systematic analysis of performance measures for classification tasks, Information Processing & Management 45 (2009) 427–437.

[47] J. A. K. Suykens, T. V. Gestel, J. D. Brabanter, B. D. Moor, J. Vandewalle, Least squares support vector machines, World Scientific, Singapore, 2002.

[48] S. Haykin, Neural Networks and Learning Machines, 3 ed., Pearson Education, New Jersey, 2009.

[49] L. Breiman, Random forests, Machine learning 45 (2001) 5–32.